Journal of Marine Research, 70, 641–660, 2012

Solar warming of near-bottom water over a fringing reef

by Judith R. Wells[1,2], Jonathan P. Fram[1] and Geno Pawlak[1]

ABSTRACT

The Kilo Nalu Observatory is located on the foreslope of a fringing reef on the south shore of Oahu, Hawaii. A cabled node at 12-m depth has enabled continuous real-time temperature observations from a thermistor chain extending from 1 to 7 m above bottom. Data from a 27-month deployment in 2007–2009 reveal repeated instances of subsurface temperature inversions. The usual diurnal pattern shows increases in temperature throughout the water column after sunrise, peaking in the early afternoon. Bottom waters typically warm faster than those at mid-depth, driving an inversion in the thermal profile. The onset and evolution of the inversions are consistent with an analytical model of radiation absorption and the contribution to bottom temperature from solar warming of the seafloor. The maximum size, duration and seasonal distribution of the inversions indicate that salinity compensation is a major limiting factor. In the absence of salinity compensation, the implication is that bottom heating destabilizes the water column and convective transport results. In addition, recurring afternoon onshore bottom currents contribute to the termination of inversions. Although radiative heating may exacerbate coral heat stress, radiation-driven thermal convection and exposure to the open ocean modulate temperatures over the reef.

1. Introduction

Coral reefs are biologically diverse, highly productive marine ecosystems. In recent decades the health of reef-building corals has been threatened by the loss of symbiotic algae and their photosynthetic pigments. This phenomenon, known as coral bleaching, can be triggered by a number of environmental factors. The most widespread events are associated with anomalously warm water (Hoegh-Guldberg, 1999; Fitt *et al*., 2001). Coral thermal tolerances vary with season and location. Most tropical and subtropical corals are exposed to maximum summer temperatures that come within 1–2 °C of their lethal limits (Coles *et al*., 1976). Fluctuating, as well as steady, exposure to high temperature can adversely affect coral health (Putnam and Edmunds, 2011). Even temperatures below the bleaching threshold, but above normal, can impair skeletal growth and reproduction (Jokiel and Coles, 1990).

Large-scale bleaching events in Hawaii in 1996 were associated with a prolonged 1 °C elevation in regional sea surface temperature (SST). Bleaching was observed on reef flats

1. Department of Ocean and Resources Engineering, 2540 Dole Street, University of Hawaii, Honolulu, Hawaii, 96822, U.S.A.

2. Corresponding author. ***email: wellsjr@hawaii.edu***

and in bays—shallow areas with restricted circulation where strong insolation, low winds and low turbidity combined to increase inshore water temperature by 1–2 °C (Jokiel and Brown, 2004). Heat stress experienced by coral colonies may have been further intensified by direct radiation. Laboratory and field experiments demonstrate that, under low-flow, clear-water conditions, solar radiation raises coral surface temperatures 0.2–1.5 °C above the ambient water (Fabricius, 2006; Jimenez *et al.*, 2008).

The reefs in the main Hawaiian Islands are commonly fringing reefs. Offshore of the reef flats and crest, the fore reef extends to about the 40-m depth. Fore-reef waters are subject to the same atmospheric forcing as back-reef waters and are also exposed to vigorous physical forcing from the open ocean, including wind and tidally driven currents, surface waves and internal tides. Coral species diversity is highest at depths between 10- and 20-m, where sufficient light reaches the seafloor and wave-induced stress is damped (Dollar, 1982; Grigg, 1983, 1998). Recent observations of temperature inversions on the fore reef at the Kilo Nalu 12-m site suggest that solar radiation penetrating to that depth is strong enough to heat the seafloor and affect the thermal environment of benthic organisms. The sections that follow describe these observations and present a model to account for heat increases through absorption of solar radiation in the water column and at the seafloor. The process is examined through the detailed analysis of one inversion episode and an overview of the full data set. Salinity compensation is considered as a factor limiting the magnitude of temperature inversions. Thermally driven cross-shore currents are discussed as a factor limiting the duration of the inversion episodes.

2. Materials and methods

a. Observation site and data sources

The Kilo Nalu Observatory is a cabled coastal monitoring and research station located off the south shore of Oahu at 21.29 °N, 157.86 °W (Fig. 1). The topography and open ocean exposure at this location are representative of subtropical fore reefs. The substrate consists largely of Holocene limestone reef with regions of extensive live coral interspersed with patches of carbonate sands (Ferrall, 1976). The seafloor is characterized by a fairly steady 1:30 slope to the 40-m isobath, after which it drops steeply, reaching the 250-m isobath within 2 km of shore.

Cabled nodes at the 12- and 23-m depths enable real-time long-term observations of currents, tides, waves and basic water quality (Pawlak *et al.*, 2009). Baseline instrumentation at the 12-m node includes a Teledyne RD Instruments (RDI) 1200-kHz Acoustic Doppler Current Profiler (ADCP) and a Precision Measurement Engineering thermistor chain (t-chain). This study uses t-chain data collected between late May 2007 and mid-July 2009 and ADCP data from 2005 through 2009. The ADCP sampled in a high-resolution mode (RDI Mode 12), recording ensemble velocity, backscatter, pressure and temperature once per second. The t-chain measured temperatures once every 4 s at 1-m intervals from 1- to 7-m above bottom (mab). The thermistors were calibrated to better than 0.01 °C and

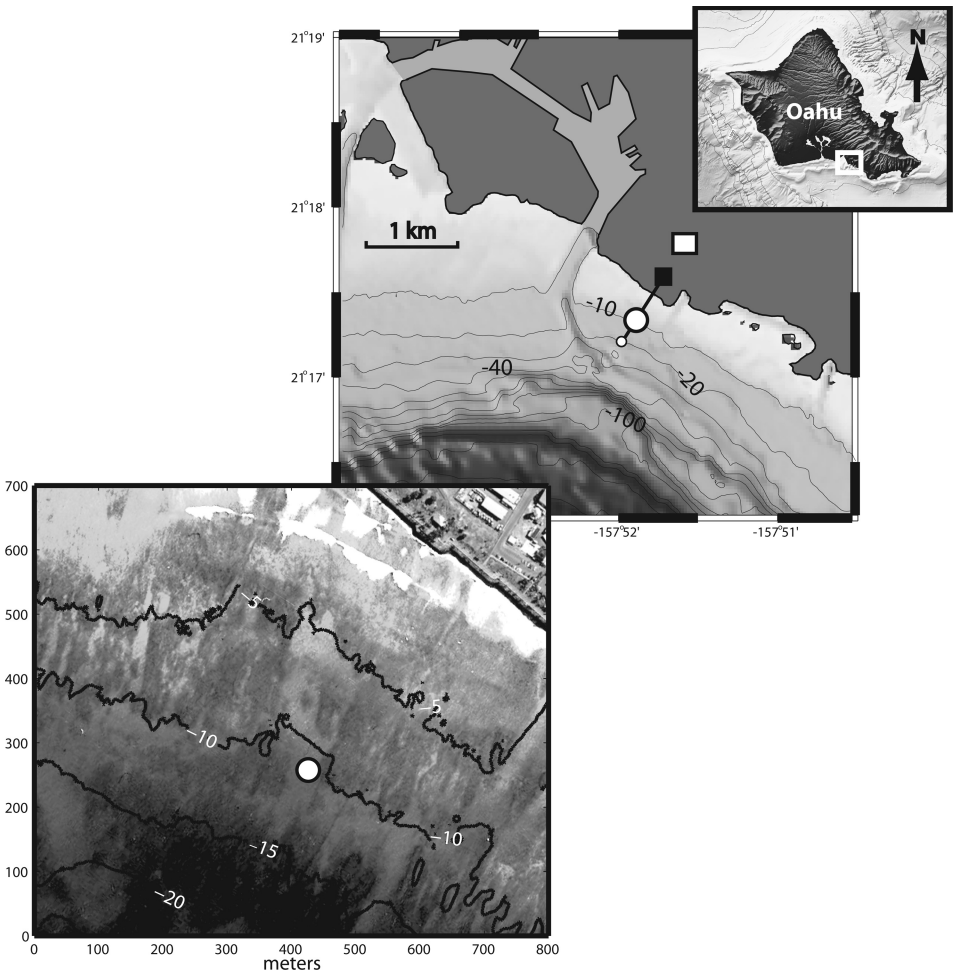

Figure 1. Kilo Nalu Observatory site on the south shore of Oahu. The symbols in the center view mark the locations of the seafloor nodes at 12 m (large white circle) and 23 m (small circle), the shore station (black square) and the meteorological station (white square). The bottom panel is a close-up of bathymetry at the 12-m site obtained from USGS SHOALS LIDAR. The contours overlie an aerial image provided by the Pacific Disaster Center.

periodically field-verified by placement at a common depth. Near-bottom salinity data were available from December 2008, when a SeaBird Electronics conductivity-temperature-depth recorder (CTD) was added to the array. The t-chain, ADCP and CTD were deployed at the 12-m isobath on a broad sand patch extending roughly 50 m by 100 m in the alongshore and cross-shore directions, respectively, surrounded by coral.

Near-surface temperature and salinity were supplied by a CTD on a telemetered surface mooring operated by the Hawaii Ocean Observing System (HiOOS). Additional information

on the spatial variability of temperature and salinity offshore and to the east of Kilo Nalu was provided through periodic surveys by a REMUS-100 (Remote Environmental Monitoring UnitS) autonomous underwater vehicle (AUV). Atmospheric data were collected at the Observatory onshore meteorological station located 800 m from the 12-m site, and supplemented with data from the National Weather Service at Honolulu Airport and stream outflow statistics from the United States Geological Survey (USGS). Measurements of solar radiation as a function of water depth were obtained from a profiling CTD equipped with a Biospherical Instruments Photosynthetically Active Radiation (PAR) sensor.

b. Local conditions

Astronomical tides along the south shore of Oahu have a range of order 1 m and are well predicted by the semidiurnal M_2 and the diurnal K_1 tidal components. The tidally driven currents are on the order of 0.2 m s^{-1}, predominantly alongshore and only weakly correlated with the surface tide. The M_2 constituent accounts for 30% of the current variability and the K_1 for 2%. The mean west-northwest current is typically less than 0.05 m s^{-1} (Pawlak *et al.*, 2009).

The wave climate is set by both local wind-forcing and remotely generated swell. Winds are offshore for 75% of the year, dominated by the northeasterly trades averaging 6 m s^{-1}. Short-period waves (6–8 s) with significant wave heights up to 1 m are common throughout the year from refracted easterly trade-wind swells. During winter months the winds tend to be weaker and more variable, with occasional strong southwesterlies associated with local "Kona" storms. Kona storms can generate 6- to 12-s swells with significant wave heights up to 3 m. From May to October, long-period (12- to 20-s) swells arrive from southern hemisphere storms (Pawlak *et al.*, 2009).

Bottom roughness in the vicinity of Kilo Nalu is inhomogeneous because of a mixture of bottom types (Nunes and Pawlak, 2006), with root-mean-square roughness heights of 3 cm for sand and 7 cm for coral areas (Jaramillo and Pawlak, 2011). Observations of near-bed flow dynamics over the coral substrates under varying wave conditions found enhanced dissipation within a wave boundary layer on the order of 1 m, comparable to the larger local roughness scales (Sansone *et al.*, 2008; Bandet, 2009). For the observations over sand described here, the wave boundary layer thickness is expected to be comparable to ripple heights of order 10 cm. The characteristics of the thicker, steady boundary layer associated with the steady flow are, however, influenced by roughness variations over larger alongshore spatial scales (Reidenbach *et al.*, 2006), so that effects of the rough reef beyond the local sand patch are likely to be important.

Local atmospheric data from late 2008 through 2009 show a seasonal pattern in solar radiation, air temperature and relative humidity. Typical summer-versus-winter values for daily averaged solar radiation are 300 W m^{-2} and 175 W m^{-2}. Air temperature ranges from 28 °C in summer to 22 °C in winter, and relative humidity ranges from 60% to 75%. During 2008–2009, air-sea temperature differences were typically 1–2 °C, with the air being warmer

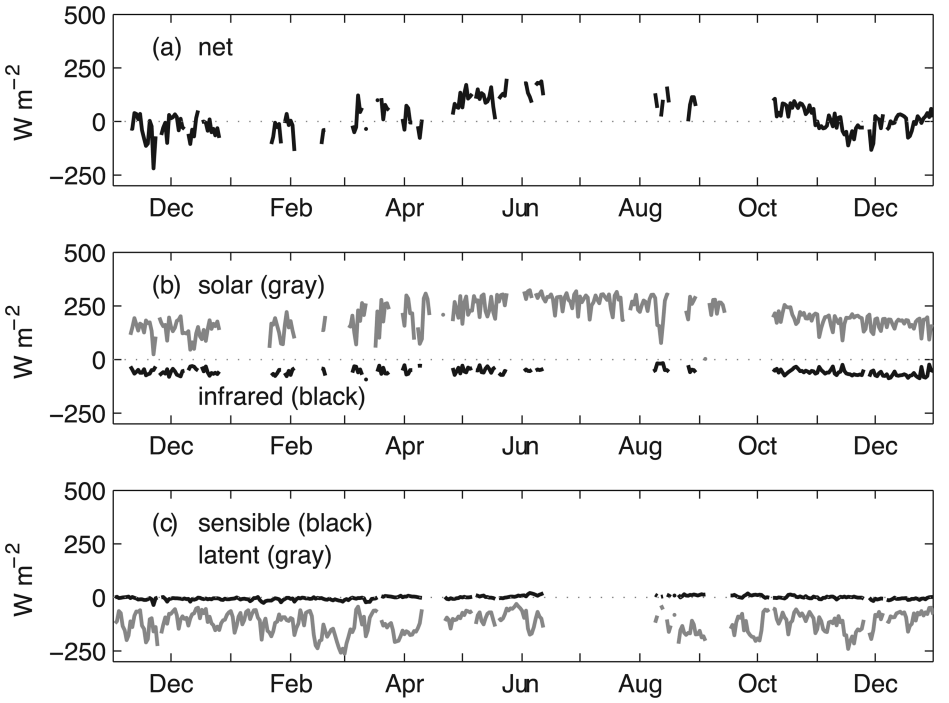

Figure 2. Net surface heat flux and its components at the Kilo Nalu 12-m site, given as daily averages for the period from November 2008 through December 2009. Positive heat flux indicates the ocean is warming. The longer gaps in the record are due to the absence of SST data during HIOOS buoy maintenance.

than the sea in the summer and colder in the winter. Bulk air-sea heat fluxes are computed from the Air-Sea Toolbox algorithms (SEA-MAT, 2006; Fairall *et al.*, 1996; Pawlowicz *et al.*, 2001). The annual pattern of surface heat flux (Fig. 2) is set mainly by the seasonal cycle of solar heating and the consistently strong evaporative cooling. Longwave (infrared) radiative cooling is an order of magnitude smaller, and sensible heat flux, which is positive in summer and negative in winter, is two orders of magnitude smaller. For the given time period, net heat flux is positive (into the ocean) from March through October, and negative from November through February.

c. Temperature trends

Water temperatures over the period of observations range between 23 and 28 °C. The annual pattern at the 12-m depth (Fig. 3) shows a seasonal modulation: coolest in February and March, warmest in July through October. The basic diurnal pattern is set by surface heat flux. Temperatures throughout the water column rise after sunrise and peak in late afternoon. Bottom waters show greater variability because of two phenomena: daytime temperature

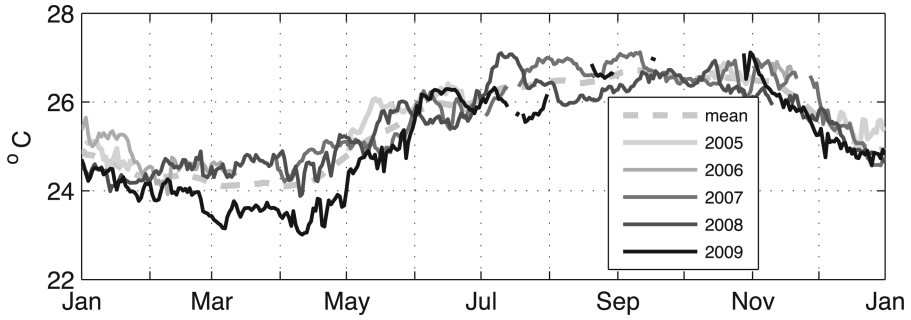

Figure 3. Daily averages of temperatures recorded by an ADCP at the 12-m depth.

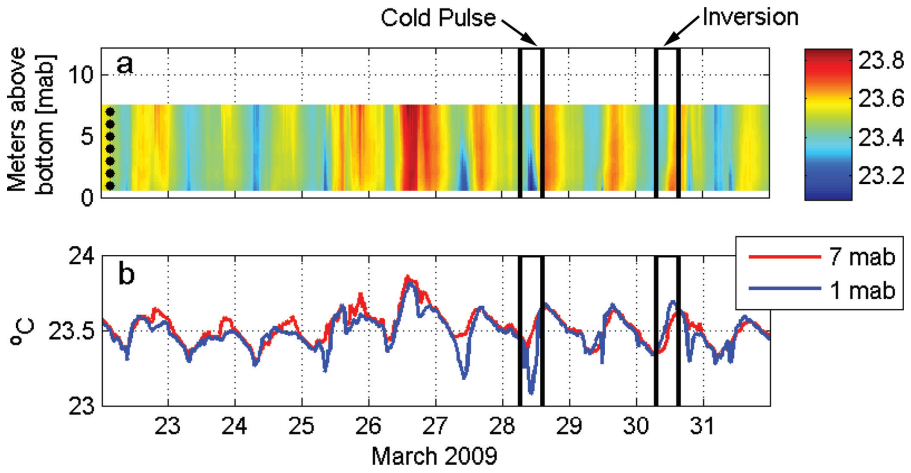

Figure 4. Diurnal temperature patterns, shown by 20-min averages of temperature recorded by the t-chain (12-m depth). (a) Data from all seven thermistors interpolated onto a finer vertical grid. Thermistor positions are indicated on the left. (b) Temperature recorded by the top (red) and bottom (blue) thermistors. Examples of a cold pulse and a temperatures inversion are indicated.

inversions and episodic cold pulses. The abrupt and transitory cold-water events tend to arrive on-site in clusters separated by days or weeks and may be a result of shoaling internal waves advecting subthermocline waters. The temperature inversions, where temperatures near the bed exceed those at mid-depth, are less dramatic but more regular. A 10-day t-chain time series from March 2009 (Fig. 4) includes multiple occurrences of both phenomena.

d. Temperature inversions

The inversions considered here are defined as temperature differences that exceed 0.025 °C over the 6-m t-chain span. They are calculated using 20-min averages from the 27-month time series (Fig. 5). A distinction has been made between inversions occurring during

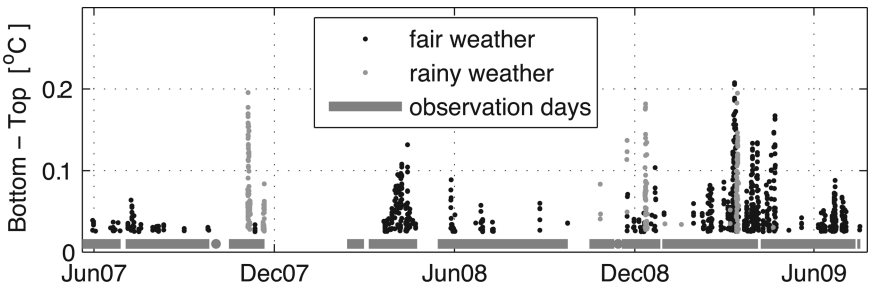

Figure 5. Magnitude of temperature inversions over the 6-m t-chain span. Each dot represents the temperature at 1 mab minus the temperature at 7 mab. Temperatures have been averaged over 20 min. Values less than 0.025 °C are excluded.

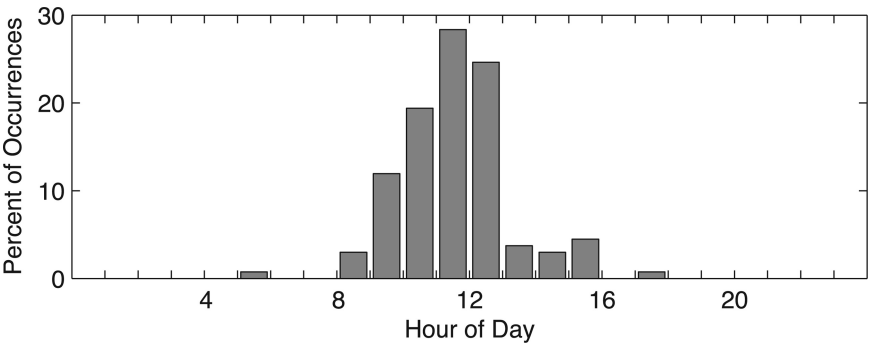

Figure 6. Distribution of daily maximum fair-weather temperature inversions by hour of day.

rainy weather (gray) and fair weather (black). Rainy days are defined as those during which the magnitude of local rainfall or stream outflow is in the top 5% of values observed for 2007–2009. The large inversions that occur during these periods are initiated and sustained by cool, fresh surface waters. The analysis that follows focuses on fair weather episodes and the phenomenon of bottom warming. On average, fair weather inversions occur on more than 20% of the days, last 2.4 hrs and reach a maximum of 0.06 °C. Most episodes reach their peak during the middle of the day (Fig. 6), a pattern consistent with heating of the water column and the seafloor by solar radiation. The average profile of inversion maxima indicates that temperatures increase monotonically with depth (Fig. 7a). In more than 75% of cases, the greatest increase in temperature occurs within the bottom 2 m. On days without inversions, midday temperatures decrease with depth (Fig. 7b).

e. Solar radiation as a function of depth

In situ PAR data, collected in 2006–2007 and in 2012, are used to evaluate the transmission of solar radiation through seawater. It is assumed that near-infrared wavelengths are

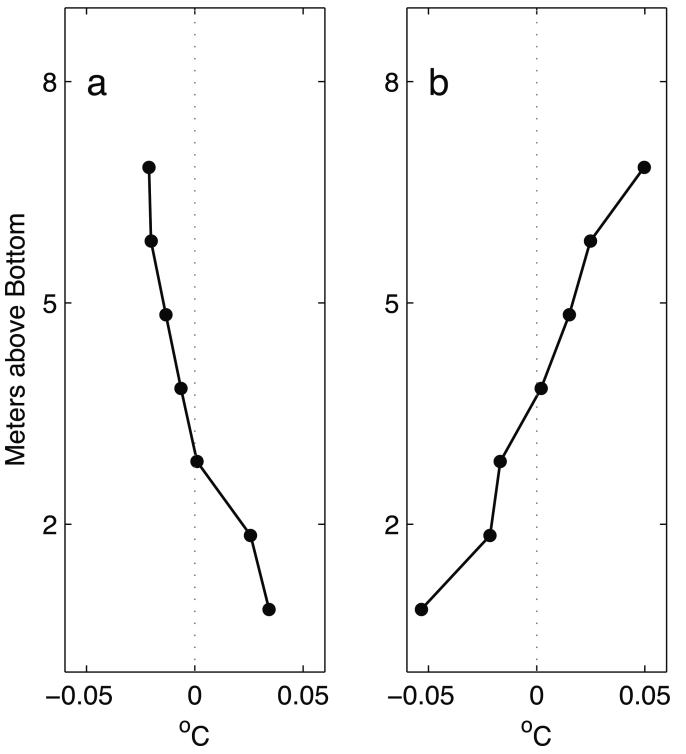

Figure 7. Profiles of average temperature (relative to the depth-averaged mean): (a) averaged over all fair-weather inversion maxima and (b) averaged over the hours from 11:00 and 13:00 on all days with no inversions.

absorbed at the top of the water column (Chang and Dickey, 2004) and that most of the energy that penetrates to greater depths is in the visible wavelengths (Ohlmann *et al.*, 1996). PAR sensors measure photon flux density (quanta $m^{-2}s^{-1}$) in the visible range, from 400 to 700 nm.

The exponential decay of light intensity I is represented by Beer's Law (Knauss, 1978),

$$I = I_0 e^{-kz}, \tag{1}$$

where I_0 is the initial radiation and z is the path length through seawater. The attenuation coefficient k is estimated from the measured change in irradiance (quanta $m^{-2}\,s^{-1}$) as a function of depth. In low-silt ocean waters, such as those at Kilo Nalu, the spectrum of photon flux density measured by a PAR sensor has a close linear relationship to energy flux per unit area (Morel and Smith, 1974). Hence the estimates of k derived from PAR data are applicable to the decay of radiant energy (W m^{-2}) and useful in evaluating water column heating.

The first PAR data set consists of three day-long series of profiles taken in mid-November 2006, late July 2007 and early August 2007 at the 12-m isobath approximately 100 m from the t-chain site (Sevadjian *et al.*, 2010). Although the PAR measurements indicate isolated instances of turbid patches within the water column, 70% of the daytime profiles show relatively smooth curves of irradiance as a function of depth. These 402 profiles are well distributed between dawn and dusk over the three days of observations, and they record similar attenuation values on each date: $k = [0.099 \pm 0.029, 0.089 \pm 0.022, 0.100 \pm 0.024]$. An additional set of profiles was collected in April 2012: one at the Kilo Nalu 12-m site and two each directly offshore at the 30-m and 40-m isobaths. The calculated attenuation is lower on this date, indicating greater optical clarity with $k = [0.063, 0.060 \pm 0.001, 0.052 \pm 0.005]$ at the 12-m, 30-m and 40-m isobaths, respectively.

In the absence of direct measurements, the attenuation of light in the water column can be estimated by the observed Secchi depth (Sd) (Pilgrim, 1984) using the formula $k = 1.7/Sd$ (Poole and Atkins, 1929). The April 2012 PAR data imply Secchi depths of [27.4, 28.3, 32.7] m. The calculations are supported by a coincident Secchi disk deployment near the deepest site showing a Secchi depth of 28 ± 1 m. The 2006–2007 data indicate average Secchi depths of [17.2, 19.1, 17.0] m with 80% of the values lying between 12 and 22 m. The range of Secchi depths is in accord with visual observations of water clarity during the 2007–2009 period. Seafloor instrumentation has usually been clearly visible from the surface at the Kilo Nalu 12-m site and frequently observable at the 23-m site.

f. Modeling the effects of solar radiation

The hypothesis is that the observed thermal inversions result from solar radiation penetrating the full-depth of the water column, heating the seafloor and increasing the temperature of near-bottom waters. The analytical model is designed to determine whether solar radiation reaching the seafloor can account for the observed inversions given realistic estimates of solar insolation, water clarity and seafloor albedo.

Light intensity I as a function of depth is modeled by Beer's Law (1), with the attenuation coefficient k determined from an estimate of the Secchi depth. The light path distance z (m) is a function of depth and the angle of surface refraction and seafloor reflection. The calculation of $\Delta I/\Delta z$ combines the downward transmission and upward reflection of sunlight with the partition between absorption and reflection at the seafloor given by the bottom albedo (A_B). The change in water temperature is then

$$\Delta T/\Delta t = 1/(\rho C_p)\Delta I/\Delta z, \tag{2}$$

where C_p is heat capacity (J kg^{-1} K^{-1}), ρ is water density (kg m^{-3}) and t is time (s).

In order to estimate the effects of seafloor absorption on water temperature, it is assumed that wave motion and currents facilitate heat transfer from the seafloor to adjacent water. Details of heat distribution will depend on boundary layer dynamics, which are not resolved in this study. In the following calculations it has been assumed that heat from the seafloor is

evenly distributed over the bottom 2 m. The choice of 2 m is based on the observed inversion profiles (Fig. 7a). Reducing the thickness of this layer would increase the estimate of solar heating at the bottom of the water column.

The application of Beer's Law for conditions characteristic of Kilo Nalu illustrates the contributions of insolation, depth, water clarity and seafloor albedo. Clear-sky insolation is computed for March 11, 2009 as a function of location and time of day, and sea surface albedo is computed as a function of solar altitude and atmospheric transmittance. On the basis of a 14-month comparison of observed insolation with theoretical zero-atmosphere transmission, typical transmittance for this location is estimated as 0.79 ± 0.02. Absorption of the incident radiation and the resultant heating are calculated for a range of bottom albedos, $A_B = [0.10, 0.25, 0.40]$, and Secchi depths, $S_d = [12, 17, 22]$ m. The values for A_B span the range of reflectance associated with seagrass, benthic algae, coral and sand-dominated substrates (Hochberg *et al.*, 2003; Mishra *et al.*, 2007). The values for S_d are restricted to optical depths that permit observable seafloor warming, i.e., $S_d \geq 12$ m, and are capped by a conservative estimate of maximum clarity.

Figure 8 shows the absorption of solar radiation for $S_d = 17$ m, $A_B = 0.25$. The absorption curves for 7:30, 9:30 and 12:30 are based on initial penetrating radiation of 180, 650 and 990 W m^{-2}, respectively, and include both the radiation transmitted from the surface and that reflected from the seafloor. Values in the bottom 2 m incorporate the radiation absorbed at the seafloor. Within the given range of A_B and S_d and in the absence of mitigating factors, such as advection and mixing, the cumulative temperature change associated with radiative absorption would produce a continuously increasing temperature inversion (Fig. 9). Lower albedo, i.e., greater absorption and less reflectance at the seafloor, leads to higher temperatures at 1 mab and slightly lower temperatures at 7 mab. For this example, the bottom-top temperature difference at the end of the day is $\Delta T = [0.42, 0.33, 0.24]$ °C for $A_B = [0.10, 0.25, 0.40]$, $S_d = 17$ m (Fig. 9a). The range of water clarity has more effect on temperature differences. Increased optical depths lead to relatively large increases in bottom temperatures and slight decreases at mid-depth. The cumulative values for ΔT are [0.04, 0.33, 0.58] °C for $Sd = [12, 17, 22]$ m, $A_B = 0.25$ (Fig. 9b).

3. Results

a. Case study of an inversion

March 11, 2009 was chosen as a test case for two reasons: the full suite of atmospheric and water column data is available and the observed temperature inversion is one of the largest fair weather events on record. The bulk air-sea heat fluxes (Fig. 10) are calculated from hourly- averaged meteorological and SST data. Figure 11 presents the t-chain data: a time series of hourly-averaged temperatures from the thermistors at 1- and 7-mab (Fig. 11a), and water column profiles at selected times (Fig. 11b–d). The depth-averaged equilibrium temperature (thick gray line, Fig. 11a) is estimated from the cumulative temperature change due to the surface forcing, relative to the observed temperature at the time of zero net heat

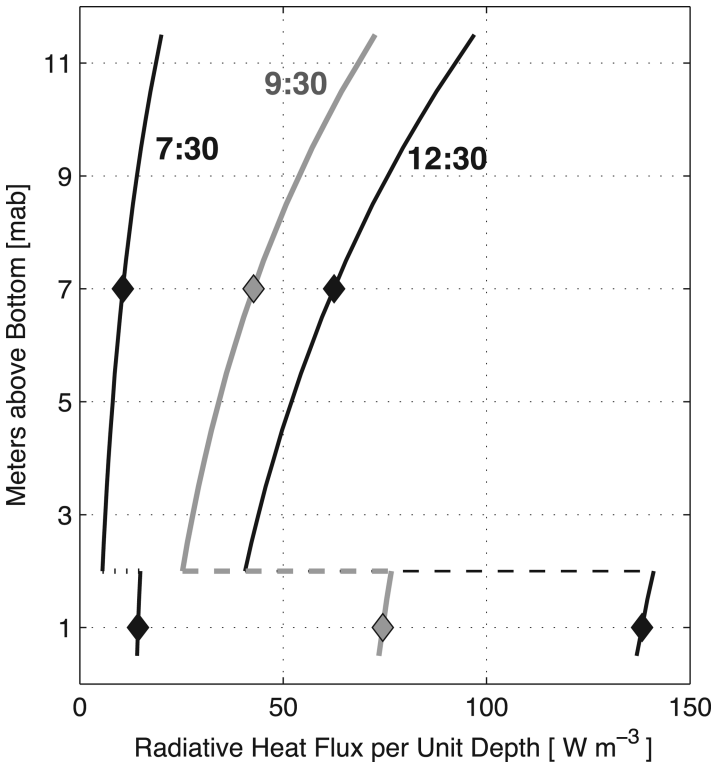

Figure 8. Calculated absorption of solar radiation (W m^{-2}) as a function of depth (m) based on Equation 1 for a 12-m depth, March 11, 2009 clear-sky insolation, seafloor albedo = 0.25 and Secchi depth = 17 m. Values in the bottom 2 m incorporate the absorption of radiation at the seafloor. Diamonds mark the position of the bottom and top thermistors at 1- and 7-mab, respectively.

flux. The lower than expected temperature observed at 7 mab at 8:30 coincides with an abrupt drop in temperature and salinity registered by the surface CTD and is possibly associated with a localized rainburst. Otherwise, mean water temperatures in the hours between midnight and early afternoon are well explained by the bulk air-sea heat fluxes. The divergence of the observed and equilibrium temperatures at 14:30 indicates advective heat flux, i.e., an incursion of a cooler water mass.

The role of solar forcing is readily identifiable, even though the factors influencing water temperature on this day include surface cooling in the morning and afternoon advective heat flux. Temperatures as a function of depth are similar before sunrise and after sunset (Fig. 11b,d), with a bottom layer 0.03 °C cooler than the nearly uniform overlying water. The profiles between 9:00 and 13:00 (Fig. 11c) document the development of the inversion. The initial inversion was partially due to surface cooling, and its eventual disappearance coincided with the arrival of the cooler water mass; its evolution was related to enhanced

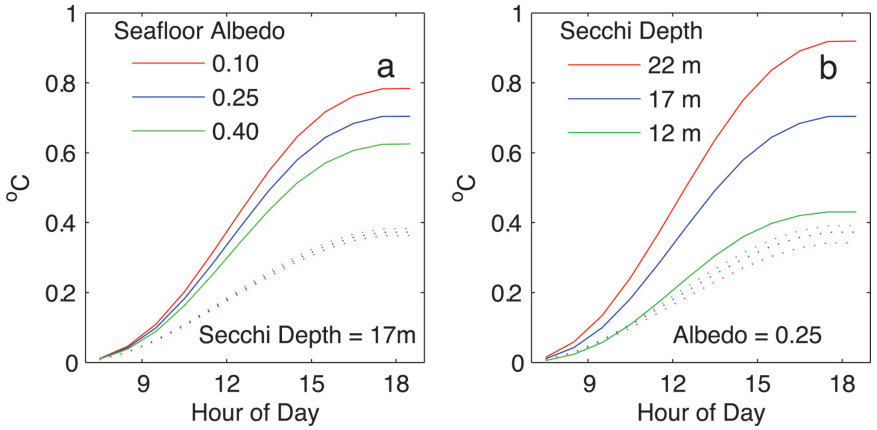

Figure 9. Theoretical effects of solar radiation based on a 12-m depth and clear-sky insolation for March 11 2009. Cumulative temperature change due to radiation (Eq. 2) based on radiation absorption curves for different values of seafloor albedo (a) and Secchi depth (b). Solid and dotted lines indicate temperatures at 1 mab and 7 mab, respectively.

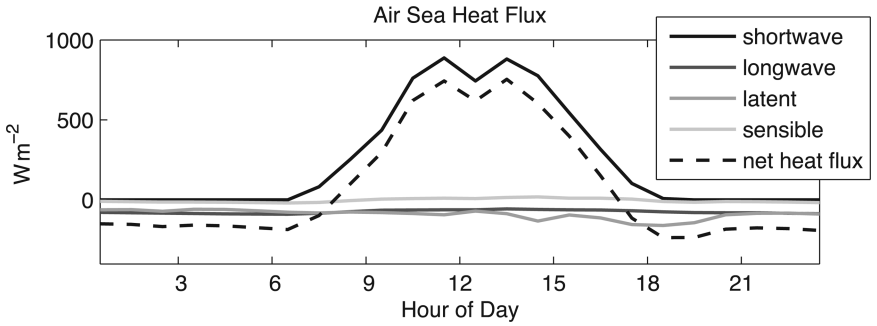

Figure 10. Air-sea heat fluxes at Kilo Nalu on March 11, 2009. Positive values represent heat into the ocean.

bottom warming. The 9:00 profile shows the initial rise of bottom temperature. The later profiles show overall warming, with temperatures at 7 mab now greater than those at 4 mab and less than those at 1 mab. The morning warming trends at both 1- and 7-mab, along with the 11:00 temperature difference (Fig. 11a) can be accounted for by the radiative heating model, using a seafloor albedo $A_B = 0.25$ and a Secchi depth $S_d = 19$ m. The model does not account for the stagnation at midday nor the erosion in inversion magnitude seen at 13:00. A key factor limiting inversion magnitude is probably water column stability as set by the combination of temperature and salinity. The eventual disappearance of the inversion may be due to the onset of instability, vertical mixing and advective cooling.

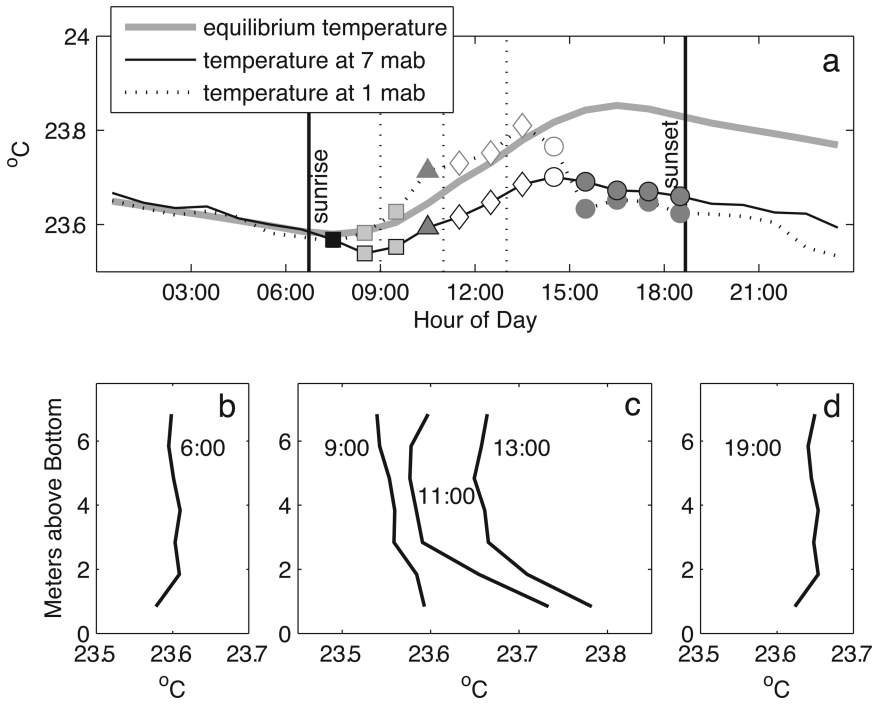

Figure 11. Hourly averaged temperatures from the t-chain at the Kilo Nalu 12-m site on March 11, 2009. (a) Water temperature at 1- and 7-mab. The symbols are for referral in Figure 12. The equilibrium temperature (thick gray curve) is calculated from the surface heat flux (Fig. 10) and has been aligned to match water temperature at the time of zero heat flux. (b,c,d) Water-column temperature profiles before sunrise, during the inversion and after sunset. Vertical lines in panel (a) mark the times.

To evaluate the role of salinity, $\Delta S/m$ and $\Delta T/m$ are calculated for March 11, assuming constant gradients in salinity between the seafloor and surface CTD and in temperature between the thermistors at 1- and 7-mab. Although the profiles are unlikely to be linear, these values are viewed as a qualitative indication of the role of ΔT versus ΔS in determining water column stability. For ΔS to balance ΔT,

$$\Delta\rho = 0 = -\alpha\Delta T + \beta\Delta S, \tag{3}$$

where ρ is density, α is the thermal expansion coefficient and β is the saline contraction coefficient. On a plot of $\Delta S/m$ versus $\Delta T/m$, the ratio α/β represents the boundary between stabilizing and destabilizing regimes (Fig. 12). The coefficients are computed for local conditions using the Seawater toolkit (Morgan and Pender 2010). For the temperature and salinity ranges on March 11, $\alpha/\beta = 0.38$, i.e., a 1 °C change in temperature is balanced by

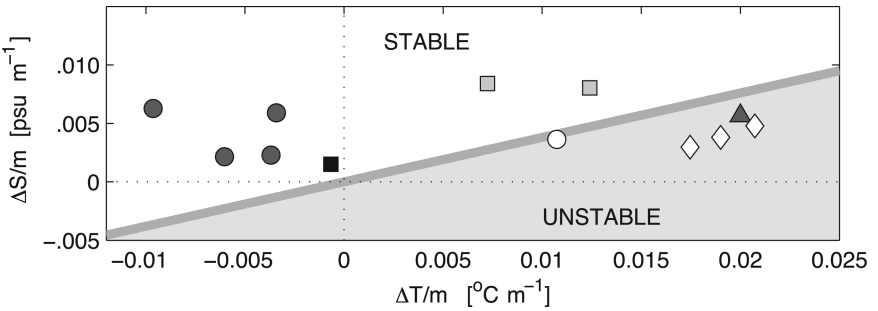

Figure 12. The relationship between ΔT and ΔS for each data point symbolized in the March 11, time series (Fig. 11a). Differences are calculated per meter based on bottom minus top values. Increasing $\Delta T/m$ is destabilizing; increasing $\Delta S/m$ is stabilizing.

0.38 psu change in salinity. The inversion is fully stable during the initial stages (squares, Fig. 11a, 12). Close to its maximum (triangle), the ΔT versus ΔS relationship becomes unstable and then the inversion begins to erode (diamonds), returning again to a stable profile (circles). A slight decrease in salinity gradient during erosion of the profile is consistent with advective/diffusive contributions. Capping of inversion magnitude is consistent with limits associated with salinity compensation.

b. Role of salinity

During the period between December 2008 and early June 2009 there were 33 inversion episodes of an hour or more for which surface and seafloor CTD data were available. Average values of $\Delta S/m$ and $\Delta T/m$ have been calculated for each episode (Fig. 13). Twenty-nine fair weather inversions are clustered near the stability boundary line, suggesting that salinity is a limiting factor in inversion growth. Four rainy day inversions highlight the stabilizing role of salinity compensation.

Uneven temporal distribution of inversions (see Fig. 5) may be attributable in part to seasonal variations in salinity. CTD data from 2009 show that bottom-top salinity differences are smaller in the summer. During the period of the coldest water temperatures in 2009, March 25 to April 10, the average salinity gradient was $\Delta S/m = 0.0042 \pm 0.0010$ [psu m^{-1}] with $\alpha/\beta = 0.38$. During the warmest period, August 19 to September 5, $\Delta S/m = 0.0016 \pm 0.0011$ and $\alpha/\beta = 0.42$. These values would support a ΔT over 6 m of 0.066 °C and 0.023 °C, respectively. Note that the latter is below the inversion threshold considered in this study. Over the 27-month t-chain deployment, inversions, as defined here, were recorded on only 7% of the days in August and September but on 46% of the days in March and April. The number of observation days in each period (110, 112) was comparable. In general, inversion episodes in winter months, November through April, are larger and longer lasting than those occurring from May through October (Fig. 14).

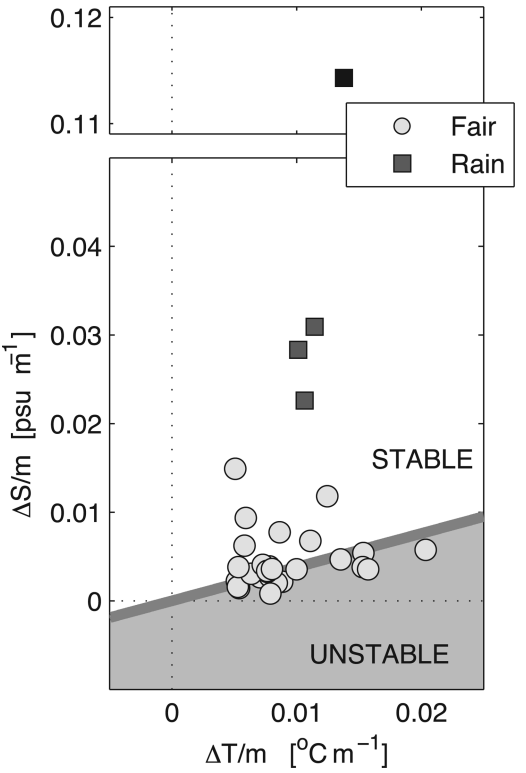

Figure 13. The relationship between average ΔT and average ΔS for inversions lasting an hour or more, Dec 2008 to Jun 2009. Differences are calculated per meter based on bottom minus top values. Increasing $\Delta T/m$ is destabilizing; increasing $\Delta S/m$ is stabilizing.

c. Role of advective heat flux

The above analysis describes temperature inversions as a one-dimensional process forced by radiative heat flux and influenced by local stratification. The influence of horizontal advection is discussed here. Full atmospheric and oceanic data sets are available for 80 days in 2009. During these times, advective heat flux is identified through a difference in slope between observed and equilibrium temperature. Hourly data indicate that the effects are gradual, raising or lowering overall temperatures by 0.15 to 0.40 °C over the course of days. All examples between April and August indicate advective cooling, whereas the examples from November through March are evenly split between cooling and warming.

Temperature inversions were analyzed with respect to onset and presence of advective heat flux, tidal phase, and depth-averaged current speed and direction. Inversion occurrence, magnitude and duration show no dependence on these environmental factors. This is probably related to the horizontal homogeneity of the temperature and salinity fields. Horizontal gradients in temperature and salinity are far smaller than vertical gradients. REMUS AUV

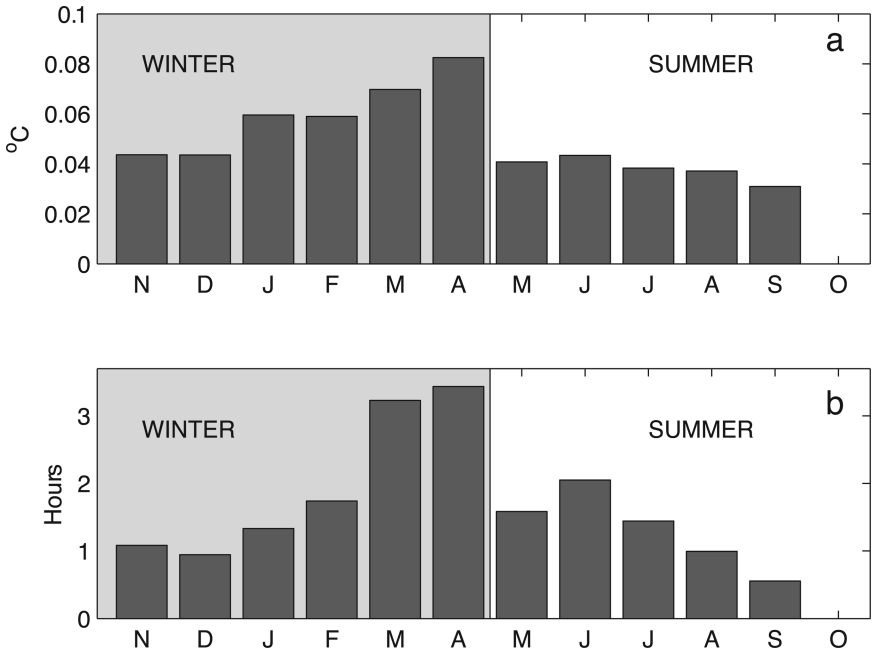

Figure 14. Monthly distribution of inversion characteristics. (a) Average episode peak magnitude (°C) and (b) average episode duration (hr). The months are ordered by season: November–April is defined as winter, May–October as summer.

surveys throughout 2009 covered the nearshore area from the Kilo Nalu site to the 50-m isobath 650 m offshore and 3.5 km east-southeast alongshore. Along the 12-m isobath, temperature and salinity gradients were O(10^{-5}) °C m^{-1} and O(10^{-6}) psu m^{-1}, as compared with surface-to-seafloor gradients at Kilo Nalu of O(10^{-2}) °C m^{-1} and O(10^{-3}) psu m^{-1}. Cross-shore gradients, measured at uniform depths, were O(10^{-4}) °C m^{-1} and O(10^{-6}) psu m^{-1}. However, near-bed waters tend to be saltier and cooler with increasing depth.

Baroclinic cross-shore currents may be a conduit for advective heat flux on the diurnal scale. Over the course of a day, the combination of convective heating from the seafloor and radiative heating from the sea surface increases vertical homogeneity and enhances the horizontal gradient between shallow and deeper locations on the reef slope. Horizontal temperature differences, in turn, can promote exchange flows across the reef such as those observed in the Red Sea (Monismith *et al.*, 2006). These flows, offshore at depth with nighttime cooling and onshore with daytime heating, would tend to reduce bottom temperature. Diurnal reversal of currents is observed at Kilo Nalu and varies with season. Between December and August, bottom onshore currents increase in strength and duration, beginning and peaking earlier in the day each month (Fig. 15). This is consistent with advective cooling of the nearshore waters and decreasing numbers of inversions during the summer

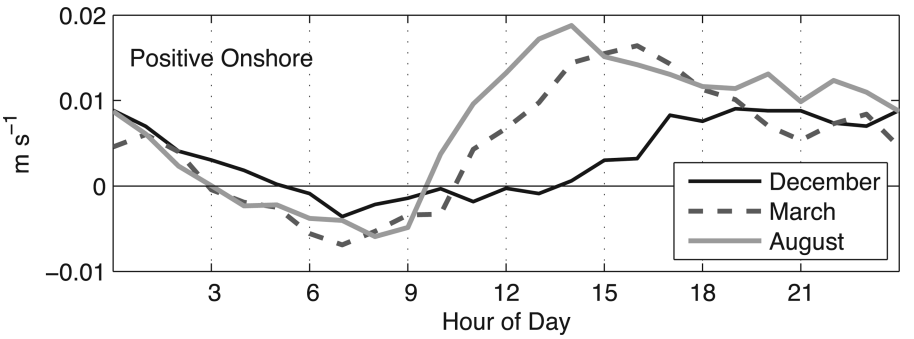

Figure 15. Cross-shore bottom currents at Kilo Nalu 12-m site. Depth is averaged over the bottom 3 m. Hourly averages for December, March and August 2007–2009.

months. In the example of March 11, 2009, near-bed currents switched from offshore to onshore at 12:30 and peaked at 15:00. During these hours the growing temperature inversion was stalled and then reversed.

4. Discussion

The t-chain record of temperature inversions supports the hypothesis that solar radiative heating of the seafloor raises bottom temperatures. Of the fair weather inversion episodes, 85% are dominated by enhanced bottom warming. In another 13%, bottom warming is evident, but inversion dynamics are ambiguous. Only 2% are clearly controlled by top-down cooling. Furthermore, observed rates of differential bottom warming are in accord with insolation data and reasonable assumptions of water clarity. Measured solar radiation in 2009 was 86% of the computed clear-sky radiation. Given strong insolation and normally clear water, solar heating of the seafloor and differential warming of bottom water can be expected to be a regular component of the thermal environment. A prolonged period of high water clarity could lead to increased coral heat stress.

On the fore-reef slope, effects of seafloor heating are mitigated by exposure to the open ocean. The vertical evolution of temperature inversions suggests that bed-driven turbulence and convective mixing play a role in the removal of heat from the seafloor and may help prevent coral from becoming significantly warmer than the ambient water. However, available data do not establish a relationship between inversion occurrences and properties and environmental factors such as current speed, wind speed and direction, and wave height and period. Further research is needed to identify their influence on the complex dynamics of turbulent diffusivity, vertical mixing and advective heat flux. Additional data on radiation incident on the seafloor, concurrent measurements of turbulent flow, and fuller vertical and horizontal data on the temperature and salinity fields would help clarify the processes that set the near-bed thermal environment and the vertical distribution of heat over the reef.

The National Oceanic and Atmospheric Administration (NOAA) Coral Reef Watch identifies thermal stress conditions on the basis of satellite-derived global nighttime SST data with a spatial resolution of 0.5 degree (∼50 km). To date, SST hot-spot indices have proven effective in assessing the threat of coral bleaching on a regional scale (Liu *et al.*, 2006). However, the present set of observations demonstrates that the classic profile of water temperature decreasing monotonically with depth is not a consistent feature of the fore reef. A study of six coral reefs in the Bahamas and the Caribbean found that temperature patterns at depth are not well captured by SST data alone. High-frequency subsurface variability due to processes such as diurnal heating, wind-driven advection and internal tides was not detected in the remotely sensed SST record (Leichter *et al.*, 2006). NOAA intends to extend its monitoring efforts to local and reef-scale events with higher resolution products and to incorporate additional environmental data such as wind, wave and solar radiation (Liu *et al.*, 2006). The temperature profiles at Kilo Nalu indicate that information on solar radiation, water clarity and depth will aid in interpreting the local impact of Coral Reef Watch SST indices.

Acknowledgments. This research has been supported by Office of Naval Research (ONR) grant N00014-06-1-0224 and National Science Foundation (NSF) grant OCE 0536616. Kilo Nalu and HiOOS operate with support from NOAA grant NA07NOS4730207. The authors would like to thank ONR, NSF, NOAA, the City and County of Honolulu and the University of Hawaii School of Ocean and Earth Science and Technology for supporting the development and utilization of the Kilo Nalu Observatory. We are indebted to Chris Colgrove, Brian McLaughlin and Kimball Millikan for invaluable contributions to field operations and data acquisition. We are grateful to Sergio Jaramillo for assistance with the REMUS CTD data, and to Eric DeCarlo, James Potemra and Michael Tomlinson for providing surface temperature and salinity data from the HiOOS mooring. We thank Jeffrey Sevadjian and Margaret McManus for sharing their PAR data, and Stephen Monismith for lending us a CTD equipped with a PAR sensor.

REFERENCES

Bandet, M. 2009. Dynamics of wave-induced boundary layers over very rough boundaries: Field observations over a stretch of coral reef. PhD thesis, University of Hawaii at Manoa, 200 pp.

Chang, G. C. and T. D. Dickey. 2004. Coastal ocean optical influences on solar transmission and radiant heating rate. J. Geophys. Res., *109*, C01020, doi: 10.1029/2003JC001821.

Coles, S. L., P. L. Jokiel and C. R. Lewis. 1976. Thermal tolerance in tropical versus subtropical Pacific reef corals. Pac. Sci., *30*, 159–166.

Dollar, S. J. 1982. Wave stress and coral community structure in Hawaii. Coral Reefs, *1*, 71–81.

Fabricius, K. E. 2006. Effects of irradiance, flow, and colony pigmentation on the temperature microenvironment around corals: Implications for coral bleaching? Limnol. Oceanogr., *51*, 30–37.

Fairall, C. W., E. F. Bradley, D. P. Rogers, J. B. Edson and G. S. Young. 1996. Bulk parameterization of air-sea fluxes for Tropical Ocean-Global Atmosphere Coupled-Ocean Response Experiment. J. Geophys. Res., *101*, 3747–3764.

Ferrall, C. C. Jr. 1976. Subsurface geology of Waikiki, Moiliili and Kakaako with engineering application. M. S. thesis, University of Hawaii at Manoa, 175 pp.

Fitt, W. K., B. E. Brown, M. E. Warner and R. P. Dunne. 2001. Coral bleaching: Interpretation of thermal tolerance limits and thermal thresholds in tropical corals. Coral Reefs, *20*, 51–65.

Grigg, R. W. 1983. Community structure, succession and development of coral reefs in Hawaii. Mar. Ecol. Prog. Ser., *11*, 1–14.

—— 1998. Holocene coral reef accretion in Hawaii: A function of wave exposure and sea level history. Coral Reefs, *17*, 263–272.

Hochberg, E. J., M. J. Atkinson and S. Andréfouët. 2003. Spectral reflectance of coral reef bottom-types worldwide and implications for coral reef remote sensing. Remote Sens. Environ., *85*, 159–173.

Hoegh-Guldberg, O. 1999. Climate change, coral bleaching and the future of the world's coral reefs. Mar. Freshw. Res., *50*, 839–866.

Jaramillo, S. and G. Pawlak. 2011. AUV-based bed-roughness mapping over a tropical reef. Coral Reefs, *30*, 11–23.

Jimenez, I. M., M. Kühl, A. W. D. Larkum and P. J. Ralph. 2008. Heat budget and thermal microenvironment of shallow-water corals: Do massive corals get warmer than branching corals? Limnol. Oceanogr., *53*, 1548–1561.

Jokiel, P. L. and E. K. Brown. 2004. Global warming, regional trends and inshore environmental conditions influence coral bleaching in Hawaii. Global Change Biol., *10*, 1627–1641.

Jokiel, P. L. and S. L. Coles. 1990. Response of Hawaiian and other Indo-Pacific reef corals to elevated temperature. Coral Reefs, *8*, 155–162.

Kantha, L. H. and C. A. Clayson. 2000. Surface exchange processes, *in* Small Scale Processes in Geophysical Fluid Flows, Academic Press, 417–509.

Knauss, J. A. 1978. Underwater optics, *in* Introduction to Physical Oceanography, Prentice-Hall, 262–267.

Leichter, J. J., B. Helmuth and A. M. Fischer. 2006. Variation beneath the surface: Quantifying complex thermal environments on coral reefs in the Caribbean, Bahamas and Florida. J. Mar. Res., *64*, 563–588.

Liu, G., A. E. Strong, W. Skirving and L. F. Arzayus. 2006. Overview of NOAA Coral Reef Watch Program's near-real-time satellite global coral bleaching monitoring activities. Proceedings of the 10th International Coral Reef Symposium, Okinawa Japan, June 28–July 2, 2004, 1783–1793.

Mishra, D. R., S. Narumalani, D. Rundquist, M. Lawson and R. Perk. 2007. Enhancing the detection and classification of coral reef and associated benthic habitats: A hyperspectral remote sensing approach. J. Geophys. Res., *112*, C08014, doi:10.1029/2006JC003892.

Monismith, S. G., A. Genin, M. A. Reidenbach, G. Yahel and J. R. Koseff. 2006. Thermally driven exchanges between a coral reef and the adjoining ocean. J. Phys. Oceanogr., *36*, 1332–1347.

Morel, A. and R. C. Smith. 1974. Relation between total quanta and total energy for aquatic photosynthesis. Limnol. Oceanogr., *19*, 591–600.

Morgan, P. and L. Pender. 2010. CSIRO MatLab SeaWater Library, Version 3.3. Data Processing Documents. [updated 18 July 2007]. Hobart, Tasmania, Australia: CSIRO Marine Research, CSIRO Australia. Available at http://www.marine.csiro.au/datacentre/processing.htm

Nunes, V. and G. Pawlak. 2008. Observations of bed roughness of a coral reef. J. Coast. Res., *24*, 39–50.

Ohlmann, J. C., D. A. Siegel and C. Gautier. 1996. Ocean mixed layer radiant heating and solar penetration: A global analysis. J. Clim., *9*, 2265–2280.

Pawlak, G., E. H. De Carlo, J. P. Fram, A. B. Hebert, C. S. Jones, B. E. McLaughlin, M. A. McManus, K. S. Millikan, F. J. Sansone, T. P. Stanton and J. R. Wells. 2009. Development, deployment, and operation of Kilo Nalu Nearshore Cabled Observatory, *in* OCEANS 2009 – EUROPE, Proceedings of a meeting held 11–14 May 2009, Bremen, Germany, IEEE, *1*, 133–142, doi: 10.1109/OCEANSE.2009.5278149.

Pawlowicz, R., B. Beardsley, S. Lentz, E. Dever and A. Anis. 2001. Software simplifies air-sea data estimates. Eos, Trans. Amer. Geophys. Union, *82*, 2.

Pilgrim, D. A. 1984. The Secchi Disc in principle and in use. The Hydrographic Journal, *33*, 25–30.

Poole, H. H. and W. R. G. Atkins. 1929. Photo-electric measurements of submarine illumination throughout the year. Mar. Biol. Assoc. U.K. J., *16*, 297–324.

Putnam, H. M. and P. J. Edmunds. 2011. The physiological response of reef corals to diel fluctuations in seawater temperature. J. Exp. Mar. Biol. Ecol. *396*, 216–223.

Reed, R. K. 1977. On estimating insolation over the ocean. J. Phys. Oceanogr. *7*, 482–485.

Reidenbach, M. A., S. G. Monismith, J. R. Koseff, G. Yahel and A. Genin. 2006. Boundary layer turbulence and flow structure over a fringing coral reef. Limnol. Oceanogr. *51*, 1956–1968.

Sansone, F. J., G. Pawlak, T. P. Stanton, M. A. McManus, B. T. Glazer, E. H. De Carlo, M. Bandet, J. Sevadjian, K. Stierhoff, C. Colgrove, A. B. Hebert and I. C. Chen. 2008. Kilo Nalu: Physical/biogeochemical dynamics above and within permeable sediments. Oceanography, *21*, 120–125.

SEA-MAT: Matlab Tools for Oceanographic Analysis. 2006. Master Index of LOCAL M-files. Matlab Index: Index for air_sea. [generated 26 April 2007]. Woods Hole, MA: USGS Coastal and Marine Geology Program, Woods Hole Science Center. Available at http://woodshole.er.usgs.gov/operations/sea-mat/index-auto.html

Sevadjian, J. C., M. A. McManus and G. Pawlak. 2010. Effects of physical structure and processes on thin zooplankton layers in Mamala Bay, Hawaii. Mar. Ecol. Prog. Ser. *409*, 95–106, doi: 10.3354/meps08614.

Received: *19 August, 2011*; revised: *21 June, 2012*.